Research Article

Experimental observation of topological large-area pseudo-spin-momentum-locking waveguide states with exceptional robustness

Liu He,[a] Zhihao Lan,[b,*] Bin Yang,[c] Jianquan Yao,[a] Qun Ren,[d,e] Jian Wei You,[e] Wei E. I. Sha,[f] Yuting Yang,[c,*] and Liang Wu[a,*]

[a]Tianjin University, Ministry of Education, School of Precision Instruments and Opto-Electronics Engineering, Key Laboratory of Opto-Electronics Information Technology Tianjin, China

[b]University College London, Department of Electronic and Electrical Engineering, London, United Kingdom

[c]University of Mining and Technology, School of Materials Science and Physics, Xuzhou, China

[d]Tianjin University, School of Electrical and Information Engineering, Tianjin, China

[e]Southeast University, School of Information Science and Engineering, State Key Laboratory of Millimeter Waves, Nanjing, China

[f]Zhejiang University, College of Information Science and Electronic Engineering, Key Laboratory of Micro-Nano Electronic Devices and Smart Systems of Zhejiang Province, Hangzhou, China

Abstract. Unlike conventional topological edge states confined at a domain wall between two topologically distinct media, the recently proposed large-area topological waveguide states in three-layer heterostructures, which consist of a domain featuring Dirac points sandwiched between two domains of different topologies, have introduced the mode width degree of freedom for more flexible manipulation of electromagnetic waves. Until now, the experimental realizations of photonic large-area topological waveguide states have been exclusively based on quantum Hall and quantum valley-Hall systems. We propose a new way to create large-area topological waveguide states based on the photonic quantum spin-Hall system and observe their unique feature of pseudo-spin-momentum-locking unidirectional propagation for the first time in experiments. Moreover, due to the new effect provided by the mode width degree of freedom, the propagation of these large-area quantum spin-Hall waveguide states exhibits unusually strong robustness against defects, e.g., large voids with size reaching several unit cells, which has not been reported previously. Finally, practical applications, such as topological channel intersection and topological energy concentrator, are further demonstrated based on these novel states. Our work not only completes the last member of such states in the photonic quantum Hall, quantum valley-Hall, and quantum spin-Hall family, but also provides further opportunities for high-capacity energy transport with tunable mode width and exceptional robustness in integrated photonic devices and on-chip communications.

Keywords: large-area quantum spin-Hall waveguide states; strong robustness against defects; high-capacity energy transport; mode width degree of freedom.

1 Introduction

The discovery of topological phases in solid-state electronic materials opened a new chapter in condensed matter physics, which has not only deepened our understanding of how topology can enrich the classification of states of matter[1] but also offered unprecedented opportunities for device applications.[2] Inspired by these exciting developments, researchers in the photonics community have made great efforts to explore the possibilities of creating topological states for photons, leading to the emerging field of topological photonics.[3–8] To date, a variety of

*Address all correspondence to Zhihao Lan, lanzhihao7@gmail.com; Yuting Yang, yangyt@cumt.edu.cn; Liang Wu, wuliang@tju.edu.cn

photonic topological states have been proposed and demonstrated, such as photonic quantum Hall states,[9–12] photonic quantum spin-Hall states,[13–16] photonic quantum valley-Hall states,[17–24] and high-order photonic topological corner states.[25,26] Due to the appealing features of photonic topological states, such as unidirectional backscattering-immune wave propagation and robustness against defects and imperfections, these states have found many interesting applications, such as robust delay lines,[27] reconfigurable waveguides,[28,29] topological quantum optics interfaces,[30] topological quantum light sources,[31] topological lasers,[32–34] and antichiral edge or surface states.[35–38]

Photonic topological edge states conventionally are created at the domain wall between two photonic crystals (PhCs) with different topologies, where the resulting edge states are tightly confined around the zero-width domain wall. To introduce the mode width degree of freedom, large-area topological waveguide states recently were proposed in three-layer heterostructures based on different topological physics,[39–47] which in general consist of a domain with Dirac points in the band structure sandwiched between two domains of gapped PhCs with distinct topological properties. The resulting topological states in these three-layer heterostructures feature uniform mode amplitudes distributed over the middle domain, whose mode width is tunable by the width of the middle domain, thus supporting high-capacity energy transport. Moreover, these large-area waveguide states enjoy similar topological properties as their domain-wall edge states counterparts, such as unidirectional propagation and backscattering immunity against certain disorders and defects, making them attractive for various applications. Specifically, Wang, *et al.*[39] were the first in experiments to demonstrate topological large-area waveguide states based on the photonic quantum Hall effect in magnetic PhCs, where the waveguide states show one-way feature with their directionality determined by the Chern number difference between the two outer domains. Later on, large-area topological waveguide states were also demonstrated in experiments based on the photonic quantum valley-Hall physics,[40] where the waveguide states show valley-locked properties with their propagation direction locked to the valley (K/K′) degree of freedom. Similar valley-locked waveguide transport has also been demonstrated in acoustic systems.[42–44] Most recently, large-area topological waveguide states were also studied theoretically based on the photonic quantum spin Hall systems,[45–47] where the resulting waveguide states show pseudo-spin-momentum-locking unidirectional propagations and can even bypass sharp bends without being backscattered.[46]

Until now, the experimental realizations of large-area topological waveguide states in photonic systems have been exclusively based on photonic quantum Hall and quantum valley-Hall systems, and the prominent feature of pseudo-spin-momentum-locking property in systems based on quantum spin-Hall effect has not been confirmed in experiments. To fill this gap, in this work, we propose a new way to create large-area pseudo-spin-locking waveguide states (LPWSs) and observe the pseudo-spin-momentum-locking unidirectional propagation in experiments for the first time. In our experiments, a domain of PhCs featuring a double Dirac-cone dispersion is sandwiched between two domains of gapped PhCs with opposite topological properties. Through numerical simulations and experimental observations, we verify that the topological waveguide modes in this setup are uniformly distributed in the middle domain and show pseudo-spin-momentum-locking unidirectional propagation.

Moreover, we also reveal an unusually strong robustness of these LPWSs against defects (e.g., cavities with sizes as large as several unit cells), which is remarkable and has not been reported previously in photonic topological systems preserving time-reversal symmetry. Practical applications of these LPWSs, such as high-energy-capacity topological channel intersection and topological energy concentrator, are also demonstrated.

2 Methods

2.1 Simulations

Full-wave simulations of this work are performed by the commercial finite-element solver, COMSOL Multiphysics 6.0. All three domains of the heterostructure are composed of PhCs with graphene-like lattice (lattice constant $a = 25$ mm), which are made of dielectric alumina cylinders with relative permittivity $\varepsilon(r) = 7.5$ and radius of $0.12a$. To calculate the photonic band structures of the three lattice cell units in the first Brillouin zone, as shown in the right panels of Fig. 1(b), periodic boundary conditions are imposed on the opposite edges of the hexagonal unit cell. To calculate the projected photonic band structures along wave vector k_x, periodic and perfect electric conductor boundary conditions are applied to the x and y directions of the supercell A|B$_x$|C, respectively, where domains A and C are fixed to have 11 lattice unit cells, whereas domain B has a width of $x = 0, 1, 3, 5, 7, 9, 11$. The calculated results are shown in Fig. S2 in the Supplementary Material. For the simulations of finite PhC structures, all computational domains are surrounded by scattering boundary conditions. The simulated field amplitude or geometric structures are shown in Figs. 1(d)–1(f), Figs. 3(a)–3(h), and Figs. 4(a)–4(c).

2.2 Experimental Measurements

The PhC samples composed of alumina cylinders are assembled inside two parallel metallic plates, and transverse magnetic ™ polarization is studied in the experimental measurements. In the microwave field mapper system, a chiral source is placed in the bottom plate through a drilled hole, and the time-harmonic field distributions are measured by a probing antenna connected to a vector network analyzer (Keysight E5063A) through the top metallic plate. To guarantee a smooth movement of the top plate in automatic measurements, there is a small air gap between alumina cylinders and the top plate.

3 Model Setup and Result Discussion

The heterostructure A|B$_x$|C considered in this work consists of three PhCs, i.e., domains A, B, and C, whose unit cells contain six alumina cylinders with dielectric constant $\varepsilon(r) = 7.5$ and radius $0.12a$ embedded in the air [see Fig. 1(a)]. Here, x denotes the width (number of unit cells) of domain B, where a is the lattice constant. To simplify the experimental realization, we fix the positions of the first, third, and fifth cylinders at a distance $R_1 = 1/3a$ from the unit cell center, whereas changing R_2 of the second, fourth, and sixth cylinders is sufficient to induce a topological phase transition for constructing the topological heterostructure. Note that we only focus on the TM modes with nonzero (E_Z, H_X, H_Y) in this work. Specifically, as shown by the band structures of the three domains in the right panels of Fig. 1(a), when $R_1 = 1/3a$ and $R_2 = 1/3.5a$, the eigenmode of the PhC at Γ point below (above) the bandgap exhibits $p_\pm$ ($d_\pm$) property, and thus is trivial. For $R_1 = R_2 = 1/3a$, a fourfold
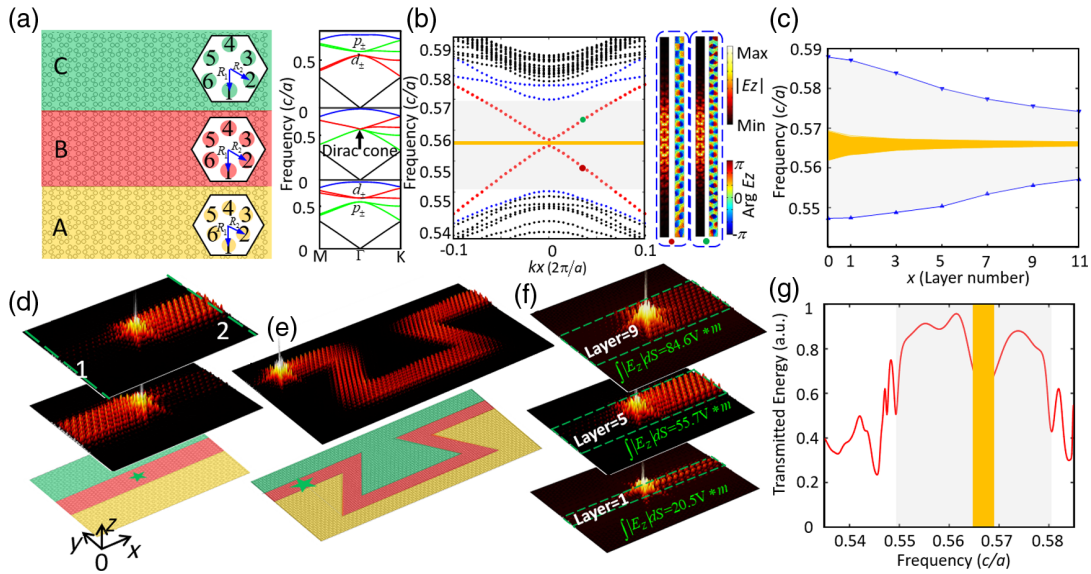
Fig. 1 Setup for LPWSs. (a) Schematic (left) of the three-layer heterostructure $A|B_x|C$ and the corresponding band structures (right) of the domains A, B, and C. Here, x labels the width (number of unit cells along y) of the middle domain B, and unit cells of the three domains are highlighted as insets. (b) Projected band structure along k_x for $A|B_5|C$, where the black, blue, and red dotted lines denote bulk, nontopological waveguide, and topological waveguide modes, respectively. The amplitude and phase distributions of the topological waveguide modes (E_Z) marked by red and green dots are shown on the right. (c) Width of the topological frequency window (marked by the light shadow in (b) as a function of x, where the light orange region marks the small gap between the two branches of topological waveguide modes. (d) Simulated $|E_Z|$ distributions of the pseudo-spin-momentum-locking unidirectional propagation at frequency $0.5601 c/a$ in $A|B_5|C$, where the chiral source for excitation is marked by the green star. (e) Simulated $|E_Z|$ distribution of the topological propagation against four sharp bends in an Ω-shaped waveguide at frequency $0.5601 c/a$ using $A|B_5|C$. (f) Simulated $|E_Z|$ distributions of the topological waveguide modes at frequency $0.5627 c/a$ for $x = 1, 5$, and 9, where the green dashed lines highlight the boundaries of domain B. (g) Simulated transmission spectrum versus frequency in a straight waveguide with $x = 5$, where the light and orange regions denote the topological frequency window and topological mode gap, respectively.

degeneracy at the Γ point forms, leading to the appearance of a gapless double Dirac cone. For $R_1 = 1/3a$, $R_2 = 1/2.65a$, the eigenmode of the PhC at Γ point below (above) the bandgap exhibits $d_\pm$ ($p_\pm$) property, indicating a band inversion compared to the trivial PhC, and thus is topologically nontrivial (more details about the band inversion and topological phase transition in this model, as well as a tight-binding description, can be found in Note 1 in the Supplementary Material). These three PhC structures are convenient for constructing the heterostructure that supports LPWSs, as we will show in the following.

The projected band structure of a heterostructure $(A|B_5|C)$ constructed using the parameters discussed above is shown in the left panel of Fig. 1(b), from which one can see that a pair of waveguide modes (red dots) exhibiting the typical helical feature of conventional pseudo-spin-Hall edge states, i.e., at each frequency there are two modes with opposite group velocities and thus opposite propagation directions, emerge within the bulk bandgap (light shaded region) of domains A and C. The mode amplitude and phase distributions of two representative states (marked by green and red dots in the projected band structure) are presented on the right of Fig. 1(b), which show that while the mode amplitudes ($|E_Z|$) of the modes are uniformly distributed in the middle domain B, their phase distributions

exhibit pseudo-spin chirality-locking property. These results indicate that our designed heterostructure supports LPWSs. The topological frequency window within which the topological waveguide modes reside as a function of the width x of the middle domain is shown in Fig. 1(c). As expected, when x increases, the size of the topological frequency window decreases due to the weakened coupling among the interface modes at A|B and B|C domain walls as well as the bulk modes in domain B. Furthermore, the small gap (light orange region) between the two branches of topological waveguide modes becomes narrower as x increases because the symmetry mismatch between domains A and C is mitigated by inserting domain B, whose parameters interpolate between those of A and C. Note that the small gap between the two branches of topological waveguide modes could be reduced by using a graded transition zone[48], or even truly gapless topological waveguide modes may be realized by using more complicated Kekule distortion.[49,50] Apart from the topological waveguide modes, we note that there are also gapped nontopological waveguide modes appearing within the bulk bandgaps of domains A and B [see the blue dots in the band structure of Fig. 1(b) and their detailed characterizations are given in the Notes 2 and 3 in the Supplementary Material].

To demonstrate the pseudo-spin-momentum-locking feature of the topological waveguide modes, their propagations excited by a chiral source marked by the green star at frequency $0.5601c/a$ are shown in Fig. 1(d) (in the simulations, three dipoles with phase winding of $2\pi/3$ along the clockwise or anti-clockwise direction are used as the circularly polarized excitation source), where clear unidirectional propagation behaviors can be observed. Moreover, to demonstrate that the unidirectional propagation is topological with respect to the crystalline symmetry, i.e., possessing immunity against sharp bends, we construct an omega-shaped waveguide in Fig. 1(e); the result shows that the excited wave can bypass four sharp bends without noticeable backscattering. The unidirectional propagations at frequency $0.5627c/a$ with different mode widths of $x = 1$, 5, and 9 are shown in Fig. 1(f), and for all three cases, the energy of the field is highly concentrated in domain B. The energy capacity of the modes with different x could be obtained by integrating the E_Z field along the waveguide cross section marked by the green dashed rectangle in Fig. 1(f), and the results show that the energy capacity carried by the mode could be tuned by varying the width x of domain B. Finally, the transmission spectrum of the waveguide structure A|B$_5$|C is further studied. The energy of the electromagnetic wave that passes through the planes 1 and 2 [indicated by the white dashed lines in Fig. 2(c)] can be calculated by $U = 1/2 \int_l \text{Re}(\vec{E} \times \vec{H}*) \cdot dl$, from which we can define the percentage of transmitted energy as $U_2/(U_1 + U_2)$; the results are shown in Fig. 1(g), from which one can see that the topological waveguide modes show high directionality within the topological frequency window (note that the drop in transmission marked by the orange region

is due to the small gap between the topological waveguide modes).

4 Experimental Observations of LPWSs

Microwave experiments are performed to demonstrate the pseudo-spin-momentum-locking unidirectional propagation and robustness against disorders and defects of the large-area topological waveguide modes. A photograph of an experimental sample from the top view is shown in Fig. 2(a), where all parameters of PhCs are the same as those simulated in Fig. 1, and the lattice constant is $a = 25$ mm in the experiments. The chiral source for launching right-propagating electromagnetic waves in domain B ($x = 5$) is constructed by three antennas with a phase difference of $2\pi/3$ between neighboring antennas along the clockwise direction. The whole PhC heterostructure is surrounded by absorbing materials (in blue) to avoid unwanted scattering (more details about the experimental setup can be found in Sec. 2.2). To demonstrate the hallmark feature of pseudo-spin-momentum-locking unidirectional propagation, we put the chiral source in the middle of the waveguide and present the measured amplitude of the E_Z field in the experiment at frequency of 7.92 GHz in Fig. 2(b). The result shows that the excited wave propagates unidirectionally to the right, while its field is mainly confined in the middle domain, which agrees with the simulation results in Fig. 1(d). Note that due to the time-reversal symmetry of the helical waveguide modes, flipping the chirality of the source in Fig. 2(b) will excite wave propagating unidirectionally to the left (not shown). To verify that the propagation of the topological waveguide modes is
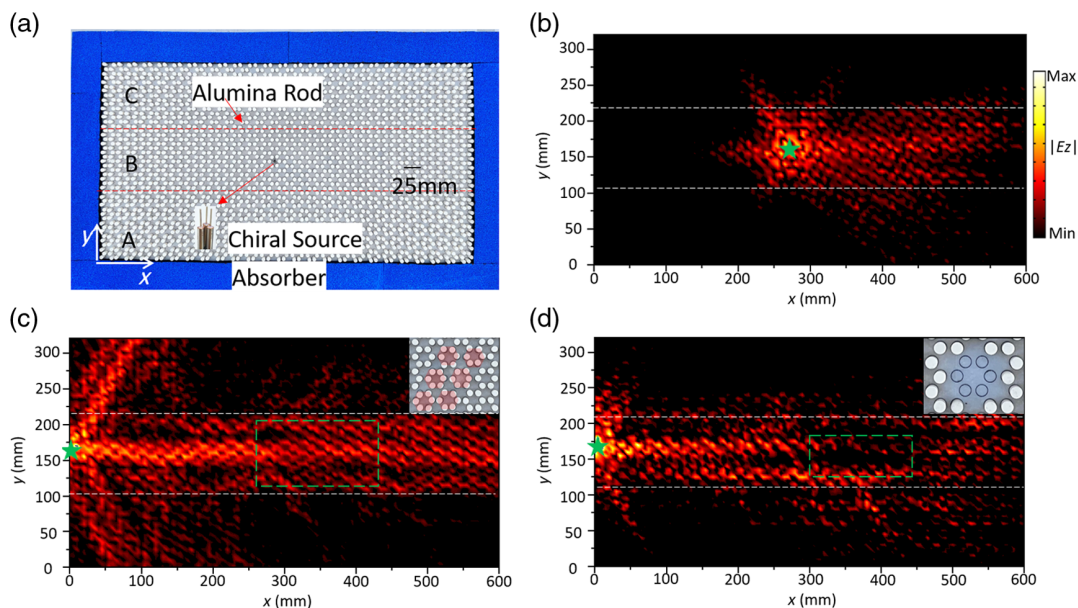

Fig. 2 Experimental observations of LPWSs. (a) Photograph of an experimental sample from the top view, where the red dashed lines denote interfaces A|B and B|C, respectively, and all alumina cylinders are surrounded by microwave-absorbing foams (blue regions). The chiral source is composed of three antennas with phase winding $2\pi/3$ along the clockwise direction, which is placed parallel to the alumina cylinders for launching the EM wave. (b) Measured amplitude of the E_Z field at frequency of 7.92 GHz with source location indicated by the green star. (c) and (d) Measured amplitudes of the E_Z field at frequency of 8.02 GHz for two different structural imperfections—disorder in (c) and a void cavity in (d), where the green dashed rectangles highlight the positions of the imperfections in experiments (see the top-right for details).

robust against disorder and defects, we introduce random shifts of the cylinder positions and a void cavity within a certain region of B in the fabricated samples. The measured amplitude of the E_Z field in Fig. 2(c) shows that despite the disorder (within the green dashed rectangle) along the propagation path, the excited wave (source location marked by a green star) can bypass the disordered region without being backscattered. Similarly in Fig. 2(d), the propagation of the excited wave can bypass a region with a void cavity without being backscattered (for more discussions about the robustness of the topological waveguide modes against disorder and defects, see Note 8 in the Supplementary Material).

5 Strong Robustness of LPWSs against Large Defects

While the conventional photonic helical edge states show some robustness against certain disorders and defects, it crucially depends on the location and type of the disorders and defects. For example, as the amplitude of the conventional edge states decays exponentially away from the interface, disorder or defects located more closely to the interface in general will affect the wave propagation more significantly than disorders or defects

located far away from the interface. Moreover, as the symmetry protecting the photonic helical edge states is emulated by crystalline symmetry, any disorders or defects will break this symmetry in principle and can destroy the topological protection.[14] The width degree of freedom of the large-area topological waveguide modes makes the realization of stronger robustness possible because the amplitude of the LPWSs is uniformly distributed in the middle domain, and as such, one can expect if the transverse dimension of the defect is smaller than the mode width, its effect on the wave propagation will also be small. As the mode width can be tuned to be arbitrarily large by increasing the width of the domain B, the large-area topological waveguide modes have the potential to be immune against much larger defects.

To understand the effect of transverse dimension of the defect on the backscattering of propagation of LPWSs, we first study the air cavity (a cluster of dielectric cylinders being removed) with increasing transverse dimension while fixing the mode width (i.e., the width of the middle domain B) to be $x = 5$. From the simulation results shown in Figs. 3(a)–3(d), we can see that the unidirectional propagation of the topological waveguides modes can bypass C1, C2, and C3 air cavities, whereas being completely backscattered by C4 air cavity due to its large
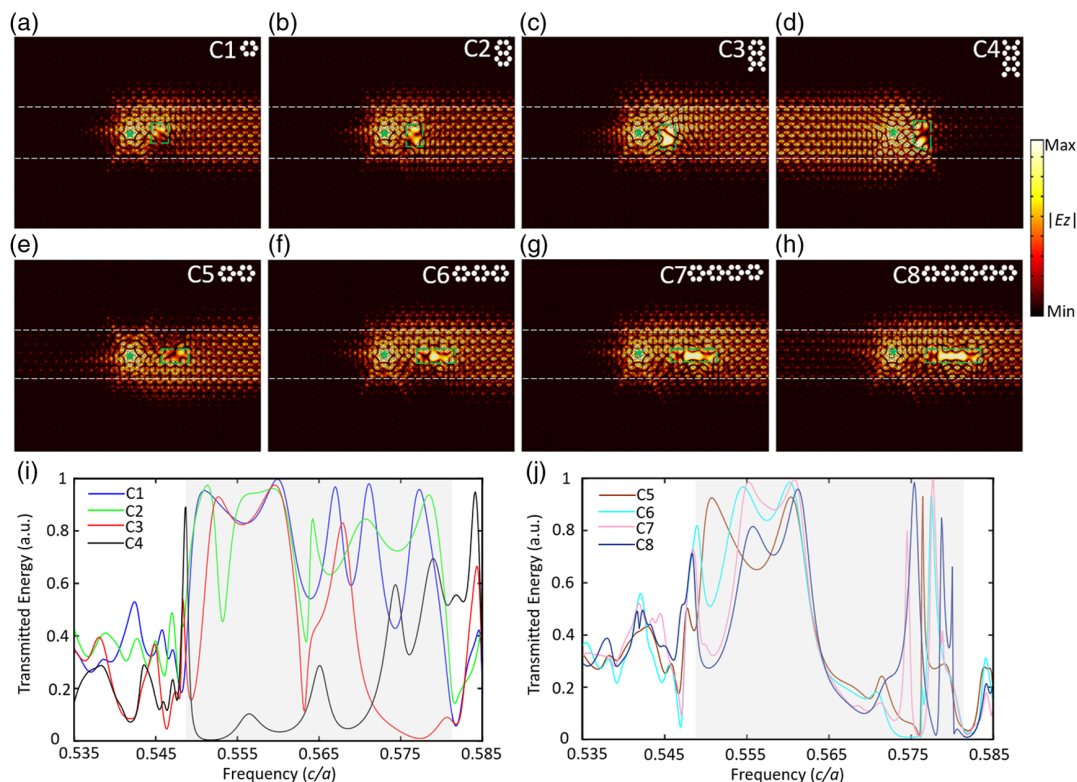

Fig. 3 Strong robustness against large cavity defects of the LPWSs. (a)–(d) Simulated propagation of the topological waveguide modes with cavity defects along the propagation path in A|B$_5$|C waveguide at frequency 0.5601c/a. The size of the cavity defects increases along the transverse direction from (a)–(d) (see schematics of the insets). The white dashed lines denote the boundaries of the domain B, and the green dashed rectangles highlight the location of the air cavities. (e) and (h) Similar to (a)–(d), but for cavity defects with size increasing along the longitudinal direction (see the schematics of the insets). (i) Transmission spectra versus frequency for the waveguides with different cavity defects in (a)–(d). (j) Transmission spectra versus frequency for the waveguides with different cavity defects in (e)–(h).

transverse size, which agrees with our reasoning above. To further demonstrate that it is the transverse size of the cavity that plays the key role in blocking the unidirectional propagation of the topological waveguide modes, we present in Figs. 3(e)–3(h) the simulation results of another series of air cavities with fixed transverse size of 1 unit cell whereas with different longitudinal sizes of 2, 3, 4, and 5 unit cells (see the insets for their geometries). The results show that increasing the longitudinal size of the air cavity has a negligible effect on the unidirectional propagation of the topological waveguide modes [Poynting vector distributions of Figs. 3(a)–3(h) are given in Fig. S10 in the Supplementary Material]. To the best of our knowledge, the enhanced robustness of the topological waveguide modes against large defects due to the mode width degree of freedom has not been studied previously, which provides an exciting new opportunity for more robust wave manipulation. The transmission spectra of the waveguides with different air cavities in Figs. 3(a)–3(d) and Fig. 3(h) are presented in Figs. 3(i) and 3(j), respectively. From the results shown in Fig. 3(i), we can see that at lower frequencies, below $0.56c/a$ within the topological frequency window, the propagation shows relatively high transmission for C1, C2, and C3 air cavities, whereas at higher frequencies, due to resonance of the cavities, the transmission shows oscillations. For the C4 air cavity, the transmission is much smaller due to the large transverse size of the cavity that blocks the wave propagation. For the transmission spectra shown in Fig. 3(j) for waveguides with increasing size of cavity along the longitudinal direction, the transmissions for all the cases show a similar feature in the middle of the topological frequency window where the topological property of the LPWSs is more prominent. Our results thus demonstrate a new scenario in which the mode width degree for freedom of the topological waveguide modes can tolerate much larger defects compared with conventional topological edge states with zero mode width.

6 Applications

The prominent features of LPWSs, such as pseudo-spin-momentum-locking unidirectional propagations and exceptional robustness against much larger defects due to the mode width degree of freedom, make them promising for high-capacity energy transport in waveguide-based integrated photonic devices and circuits.

To demonstrate the application potentials of LPWSs, we first design a topological channel intersection using the pseudo-spin-momentum-locking property of LPWSs as shown in Figs. 4(a) and 4(b), where four ports labeled as 1 to 4 are used for wave routing with a waveguide width (i.e., width of domain B) of $x = 5$, and the white dashed lines denote the interfaces between different domains (see Note 11 in the Supplementary Material for its geometrical structure). The simulated performances of the topological channel intersection when the chiral source is located at ports 1 and 3 are presented in Figs. 4(a) and 4(b), respectively. From the results, we can see that when the chiral source is located at port 1 (port 3), the launched topological guided modes can only propagate to ports 3 and 4 (ports 1 and 2) and are suppressed in port 2 (port 4). This is because, when the chiral source is placed at port 1 (port 3), the transport channels from port 1 to ports 3 and 4 (from port 3 to ports 1 and 2) have the same chirality, which is different from the chirality of transport channel from ports 1 to 2 (from port 3 to 4); thus the transport is suppressed from port 1 to 2 (from port 3 to 4). The transmission spectra of the two cases are calculated and presented in Figs. 4(d) and 4(e), where the transmission from port i to port j is labeled as Pji. From the results, we can see that the transmissions of P31 and P41 (P13 and P23) are much larger than that of P21 (P43) within the operational bandwidth when the chiral source is at port 1 (port 3), demonstrating the high efficiency of the designed topological channel intersection with finite waveguide width.
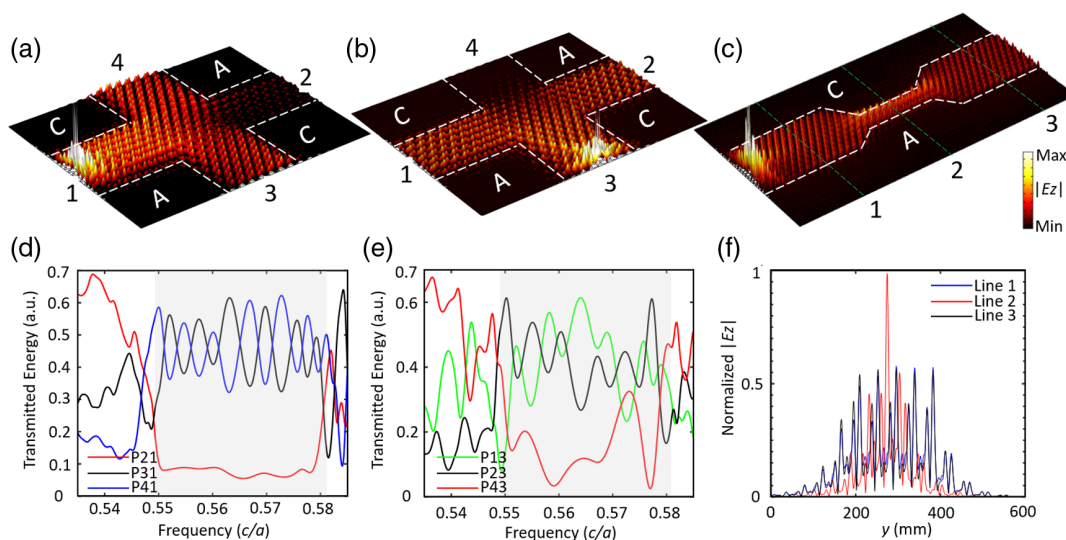

Fig. 4 Applications of LPWSs. (a) and (b) Simulated amplitudes of the E_z field in topological channel intersections using LPWSs, where the chiral source is placed at port 1 and port 3 in (a) and (b), respectively. (c) Simulated amplitude of the E_z field in topological energy concentrator using LPWSs. (d) and (e) Transmission spectra corresponding to (a) and (b). (f) Normalized $|E_z|$ profiles along three dashed green lines in (c).

Furthermore, a topological energy concentrator using the LPWSs is further designed and studied in Fig. 4(c), where the width of domain B changes from $x = 9$ to $x = 1$ along the propagation path. From the result, one can see that the energy of the wave in the wide channel of domain B gradually evolves into the narrow channel in the middle part of the waveguide and then expands back during the later stage of the propagation. It is worth noting that the operation bandwidth of LPWSs with $x = 1$ completely covers that of LPWSs with $x = 9$, indicating that the operation bandwidth of the topological energy concentrator is determined by the wide channel of domain B. The normalized field profiles ($|E_Z|$) along three dashed green lines in Fig. 4(c) are shown in Fig. 4(f), from which one can see that the energy intensity along line 2 is much larger than those along lines 1 and 3, indicating a strong field enhancement in the narrow channel of domain B. The topological energy concentrator demonstrated here could be potentially used for field enhancement, modulating field strength, or boosting nonlinear effect. LPWSs may also be exploited for wavelength division multiplexing in waveguides with different widths of domain B, different high-capacity energy splitter/distribution,[51] and topological cavity with tunable mode confinement[40] (see Note 11 in the Supplementary Material). For example, the topological cavity with high-capacity energy transport exhibits energy peaks at certain frequencies due to the interference effect of traveling modes around the cavity,[52] which may be promising for novel topological lasing.[34]

7 Conclusions

Through both theoretical simulations and experimental observations, we have demonstrated the existence of LPWSs in a three-layer topological PhC heterostructure exploiting the photonic quantum spin-Hall effect. The LPWSs have a uniform distribution of mode amplitude in the middle domain of the heterostructure and possess prominent topological properties, such as inherent pseudo-spin-chirality, pseudo-spin momentum-locking unidirectional propagation, and tunable mode width for high-capacity energy transport. Most importantly, we have demonstrated that the mode width of the LPWSs provides a new degree of freedom for enhancing the robustness of the unidirectional propagation, which is immune to much larger defects than can be achieved for conventional topological edge states with zero mode width. The LPWSs have great potential for practical applications, such as topological channel intersections, topological energy concentrators, topological cavities with tunable mode confinement, and high-capacity energy splitters. Compared to conventional topological edge states, LPWSs are more compatible with interfacing with existing waveguide-based photonic devices, making them appealing for applications in different scenarios, such as multiband,[53] reconfigurable,[29] wavelength division multiplexing,[54,55] and coexistence of different topological states.[56,57] For future works, it would be interesting to experimentally investigate the LPWSs at higher frequencies, such as terahertz, infrared, and optical frequencies, for more compact on-chip applications.

Disclosures

The authors declare no competing interests.

Code and Data Availability

All the data that support the findings of this study are available from the corresponding author upon request.

Numerical simulations in this work are all performed using the commercial finite-element solver COMSOL Multiphysics. All related codes can be built with the instructions in Sec. 2.

Author Contributions

Liu He: investigation, writing – original draft, validation, formal analysis. Zhihao Lan: investigation, writing – review and editing. Bin Yang: measurement in the experiment. Jianquan Yao: conceptualization, supervision. Qun Ren: review. Jian Wei You: review. Wei E. I. Sha: review. Yuting Yang: investigation, writing – review and editing, and measurement in the experiment. Liang Wu: investigation, writing – review and editing, project administration. All authors contributed to scientific discussions of the manuscript.

References

1. F. D. M. Haldane, "Nobel lecture: topological quantum matter," *Rev. Mod. Phys.* **89**, 040502 (2017).
2. O. Breunig and Y. Ando, "Opportunities in topological insulator devices," *Nat. Rev. Phys.* **4**, 184–193 (2022).
3. A. B. Khanikaev and G. Shvets, "Two-dimensional topological photonics," *Nat. Photonics* **11**, 763–773 (2017).
4. T. Ozawa et al., "Topological photonics," *Rev. Mod. Phys.* **91**, 015006 (2019).
5. G. J. Tang et al., "Topological photonic crystals: physics, designs, and applications," *Laser Photonics Rev.* **16**, 2100300 (2022).
6. Z. Lan et al., "A brief review of topological photonics in one, two, and three dimensions," *Rev. Phys.* **9**, 100076 (2022).
7. J. W. You et al., "Topological metasurface: from passive toward active and beyond," *Photonics Res.* **11**, B65–B102 (2023).
8. X. Zhang et al., "A second wave of topological phenomena in photonics and acoustics," *Nature* **618**, 687–697 (2023).
9. F. D. M. Haldane and S. Raghu, "Possible realization of directional optical waveguides in photonic crystals with broken time-reversal symmetry," *Phys. Rev. Lett.* **100**, 013904 (2008).
10. Z. Wang et al., "Reflection-free one-way edge modes in a gyromagnetic photonic crystal," *Phys. Rev. Lett.* **100**, 013905 (2008).
11. Z. Wang et al., "Observation of unidirectional backscattering-immune topological electromagnetic states," *Nature* **461**, 772–775 (2009).
12. Y. Poo et al., "Experimental realization of self-guiding unidirectional electromagnetic edge states," *Phys. Rev. Lett.* **106**, 093903 (2011).
13. A. B. Khanikaev et al., "Photonic topological insulators," *Nat. Mater.* **12**, 233–239 (2013).
14. L. H. Wu and X. Hu, "Scheme for achieving a topological photonic crystal by using dielectric material," *Phys. Rev. Lett.* **114**, 223901 (2015).
15. C. He et al., "Photonic topological insulator with broken time-reversal symmetry," *Proc. Natl. Acad. Sci. U. S. A.* **113**, 4924–4928 (2016).
16. Y. Yang et al., "Visualization of a unidirectional electromagnetic waveguide using topological photonic crystals made of dielectric materials," *Phys. Rev. Lett.* **120**, 217401 (2018).
17. T. Ma and G. Shvets, "All-Si valley-Hall photonic topological insulator," *New J. Phys.* **18**, 025012 (2016).

18. X. D. Chen et al., "Valley-contrasting physics in all-dielectric photonic crystals: orbital angular momentum and topological propagation," *Phys. Rev. B* **96**, 020202(R) (2017).
19. F. Gao et al., "Topologically protected refraction of robust kink states in valley photonic crystals," *Nat. Phys.* **14**, 140–144 (2018).
20. X. T. He et al., "A silicon-on insulator slab for topological valley transport," *Nat. Commun.* **10**, 872 (2019).
21. L. Zhang et al., "Valley kink states and topological channel intersections in substrate-integrated photonic circuitry," *Laser Photonics Rev.* **13**, 1900159 (2019).
22. Y. Yang et al., "Terahertz topological photonics for on-chip communication," *Nat. Photonics* **14**, 446 (2020).
23. H. Xue, Y. Yang, and B. Zhang, "Topological valley photonics: physics and device applications," *Adv. Photonics Res.* **2**, 2100013 (2021).
24. J. W. Liu et al., "Valley photonic crystals," *Adv. Phys. X* **6**, 1905546 (2021).
25. X. D. Chen et al., "Direct observation of corner states in second-order topological photonic crystal slabs," *Phys. Rev. Lett.* **122**, 233902 (2019).
26. B. Y. Xie et al., "Visualization of higher-order topological insulating phases in two-dimensional dielectric photonic crystals," *Phys. Rev. Lett.* **122**, 233903 (2019).
27. M. Hafezi et al., "Robust optical delay lines with topological protection," *Nat. Phys.* **7**, 907–912 (2011).
28. X. Cheng et al., "Robust reconfigurable electromagnetic pathways within a photonic topological insulator," *Nat. Mater.* **15**, 542–548 (2016).
29. J. W. You et al., "Reprogrammable plasmonic topological insulators with ultrafast control," *Nat. Commun.* **12**, 5468 (2021).
30. S. Barik et al., "A topological quantum optics interface," *Science* **359**, 666–668 (2018).
31. S. Mittal, E. A. Goldschmidt, and M. Hafezi, "A topological source of quantum light," *Nature* **561**, 502–506 (2018).
32. B. Bahari et al., "Nonreciprocal lasing in topological cavities of arbitrary geometries," *Science* **358**, 636–640 (2017).
33. M. A. Bandres et al., "Topological insulator laser: experiments," *Science* **359**, eaar4005 (2018).
34. Y. Zeng et al., "Electrically pumped topological laser with valley edge modes," *Nature* **578**, 246–250 (2020).
35. P. Zhou et al., "Observation of photonic antichiral edge states," *Phys. Rev. Lett.* **125**, 263603 (2020).
36. X. Xi et al., "Topological antichiral surface states in a magnetic Weyl photonic crystal," *Nat. Commun.* **14**, 1991 (2023).
37. J. W. Liu et al., "Antichiral surface states in time-reversal-invariant photonic semimetals," *Nat. Commun.* **14**, 2027 (2023).
38. Y. T. Yang et al., "Observation of antichiral edge states in a circuit lattice," *Sci. China-Phys. Mech. Astron.* **64**, 257011 (2021).
39. M. Wang et al., "Topological one-way large-area waveguide states in magnetic photonic crystals," *Phys. Rev. Lett.* **126**, 067401 (2021).
40. Q. Chen et al., "Photonic topological valley-locked waveguides," *ACS Photonics* **8**, 1400–1406 (2021).
41. S. Yan et al., "Transport of a topologically protected photonic waveguide on-chip," *Photonics Res.* **11**, 1021–1028 (2023).
42. M. Wang et al., "Valley-locked waveguide transport in acoustic heterostructures," *Nat. Commun.* **11**, 3000 (2020).
43. J. Q. Wang et al., "Extended topological valley-locked surface acoustic waves," *Nat. Commun.* **13**, 1324 (2022).
44. S. Yin et al., "Acoustic valley-locked waveguides in heterostructures of a square lattice," *Phys. Rev. Appl.* **18**, 054073 (2022).
45. Z. Hu et al., "Manipulating the optical beam width in topological pseudospin-dependent waveguides using all-dielectric photonic crystals," *Opt. Lett.* **47**, 5377–5380 (2022).
46. Z. Lan et al., "Large-area quantum-spin-Hall waveguide states in a three-layer topological photonic crystal heterostructure," *Phys. Rev. A* **107**, L041501 (2023).
47. X. Yu et al., "Topological large-area one-way transmission in pseudospin-field-dependent waveguides using magneto-optical photonic crystals," *Photonics Res.* **11**, 1105–1112 (2023).
48. R. Chaunsali et al., "Subwavelength and directional control of flexural waves in zone-folding induced topological plates," *Phys. Rev. B* **97**, 054307 (2018).
49. T.-W. Liu et al., "Nonconventional topological band properties and gapless helical edge states in elastic phononic waveguides with Kekule distortion," *Phys. Rev. B* **100**, 214110 (2019).
50. T.-W. Liu et al., "Synthetic Kramers pair in phononic elastic plates and helical edge states on a dislocation interface," *Adv. Mater.* **33**, 2005160 (2021).
51. L. He et al., "Topologically protected beam splitters and logic gates based on two-dimensional silicon photonic crystal slabs," *Opt. Express* **28**, 34015–34023 (2020).
52. Y. Yang and Z. H. Hang, "Topological whispering gallery modes in two-dimensional photonic crystal cavities," *Opt. Express* **26**, 21235–21241 (2018).
53. Q. Chen et al., "Valley-Hall photonic topological insulators with dual-band kink states," *Adv. Opt. Mater.* **7**, 1900036 (2019).
54. X. Wang et al., "Design of wavelength division multiplexing devices based on tunable edge states of valley photonic crystals," *Opt. Express* **31**, 13933–13942 (2023).
55. Y. Ruan et al., "Applications for wavelength division multiplexers based on topological photonic crystals," *Photonics Res.* **11**, 569–574 (2023).
56. M. L. N. Chen et al., "Coexistence of pseudospin- and valley-Hall-like edge states in a photonic crystal with C3v symmetry," *Phys. Rev. Res.* **2**, 043148 (2020).
57. G. Wei et al., "Coexisting valley and pseudo-spin topological edge states in photonic topological insulators made of distorted Kekule lattices," *Photonics Res.* **10**, 999–1010 (2022).

Biographies of the authors are not available.